Journal of Micromechanics and Microengineering

Memristive behaviour of electrodeposited bismuth selenide

OPEN ACCESS
IOP Publishing
Journal of Micromechanics and Microengineering
J. Micromech. Microeng. **31** (2021) 095004 (13pp)
https://doi.org/10.1088/1361-6439/ac1453

Memristive behaviour of electrodeposited bismuth selenide

I A Mihailovic*, K Klösel and C Hierold

Micro- and Nanosystems, Department of Mechanical and Process Engineering, ETH Zürich, Zürich 8092, Switzerland

E-mail: ian.mihailovic@micro.mavt.ethz.ch

Received 8 March 2021, revised 25 May 2021
Accepted for publication 14 July 2021
Published 29 July 2021

Abstract

We demonstrate memristive functions of the room temperature thermoelectric material Bi-Se fabricated by electrochemical deposition in combination with active electrode Ag-based contacts. We present microfabrication steps for creating polymer molds for the growth of compact memristive films. The electrical measurements show clear forming-free resistive switching behaviour for the electrochemically deposited material while temperature dependent measurements point to Schottky and space-charge-limited-current conduction mechanisms. For the envisioned combination of the memristors with a thermoelectric device we can conclude that electrodeposition is a viable method to produce silver-chalcogenide based non-volatile memristors for co-integration in zero power sensors.

Supplementary material for this article is available online

Keywords: memristor, resistive switching, bismuth selenide, microfabrication, electrodeposition, thermoelectric

(Some figures may appear in colour only in the online journal)

1. Introduction

The growing trends of miniaturization, reduction of power consumption and increased portability of IoT devices call for integration of components, using the same materials to perform multiple functions. If based on the same fabrication technology, this offers advantages in reduction of complexity and costs for device fabrication. In microsystems technology the co-integration of functions is applied for example for passive or zero power sensors, combining energy harvesters with sensor functions. Zhang *et al* have integrated a thermoelectric material into a microstructure capable of self-powered pressure and temperature sensing [1], while Fu *et al* used Cu-ZnO nanowires as a nanogenerator with H_2S gas sensing functionality [2]. Abunahla *et al* demonstrated the co-integration of Ag/TiO_2/Cu memristors and proposed a sensing crossbar structure to detect gamma radiation [3], while Vahl *et al* presented the concept and modelling of memsensors that respond to external stimuli [4].

Here we propose electrodeposition (ECD) as a versatile additive manufacturing technology for the fabrication of functional devices on polymeric substrates and for the co-integration of thermoelectric based heat flux sensors with a non-volatile resistive switching memory to sense and log critical values of temperature differences or heat flux. The applications are manifold, like in logistics and remote applications where constant monitoring is not typically applied [5]. The combined TEG-memristor devices therefore offer a solution between constant monitoring of quantities that requires complex battery powered electronics and single use indicators that are non-reusable and offer less flexibility when sensing external physical quantities.

A concept study with a commercial TEG (TPG-751) and first samples of electrodeposited memristors demonstrate the

* Author to whom any correspondence should be addressed.

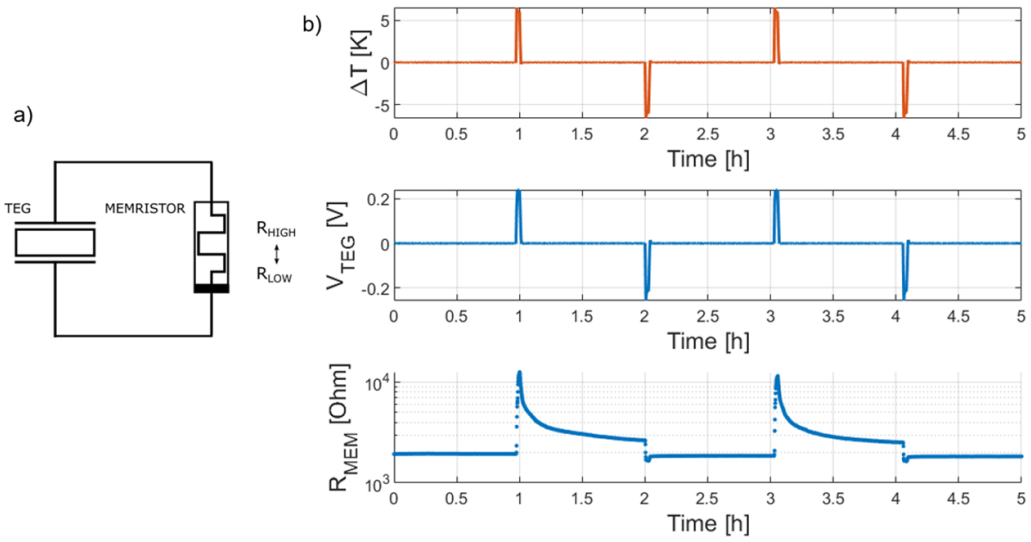

Figure 1. Concept study of the envisioned combined device. The temperature difference across a TEG directly triggers resistance changes in a memristive device.

proof of concept (figure 1) (for details see the S.I. (available online at stacks.iop.org/JMM/31/095004/mmedia)) and allow evaluating design and material options for the co-integration of TEG and memristor. The voltage output of the TEG was directly connected to the electrodeposited Ag/Bi-Se memristor as schematically shown in figure 1(a). Once the temperature difference across the thermoelectric device is sufficiently high, the TEG output voltage exceeds the memristor switching threshold, causing ion transport to change the overall resistance of the device (figure 1(b)). After the temperature difference is lowered, the resistance drops and drifts to a more stable value until an 'erase' event where a voltage of the opposite polarity is applied.

The advantages of the envisioned concept of co-integration based on microfabrication processes and electrochemical deposition yield restrictions on device design and material combinations, for example similar device thickness for the TEG and the memristor, similar lateral dimensions and material combinations that can be deposited simultaneously.

With common material selection in mind for both devices, the material should also display good thermoelectric properties. The best thermoelectric materials for operation around room temperature to date are metal-chalcogenides, such as Bi_2Te_3, Bi_2Se_3, Sb_2Te_3 and different ternary compounds of these materials [6, 7]. Among these, Bi_2Se_3 is also known to have topologically insulating properties with highly conducting topologically protected surface states, interesting for spintronics and quantum computing applications [8]. This wide range of different physical material properties make bismuth selenide interesting for autonomous sensor applications, where combined functions and compatible process flows are in demand. Memristive devices are two terminal elements where a sufficiently high external voltage can reversibly influence the internal resistance and switch it between two or more stable states. Their non-volatility and non-linearity make them attractive for use in computer memory applications [9], logic circuits [10], neuromorphic computing [11] and analogue nonlinear circuits [12]. Memristors are commonly fabricated by sputtering, CVD or ALD, however electrodeposited memristors have so far mainly been shown in oxide based CuO_x [13], ZnO [14], HfO_2, Nb_2O_5 [15] or germanium chalcogenide GeSbTe [16], GeS_2 [17] devices.

Resistive switching was also reported in Bi_2Se_3 by Tulina *et al* for sputtered and Bridgman method grown single crystals with large area millimetre sized Ag contacts [18, 19]. However, up to date, the use of ECD to fabricate Bi_xSe_y based Ag memristive devices has not been reported.

We select Bi_xSe_y and ECD for the memristor because it allows co-integration of thermoelectric based heat flux sensors and accommodate the design requirements to maintain a sufficiently high temperature difference across the thermoelectric device. ECD is commonly used to fabricate thermoelectric harvesters and sensors [20] and offers the advantage of filling small holes as well as covering larger device areas. It is a low cost, facile and scalable method that enables control over crystallinity, composition, doping and thickness by adjusting the process parameters [21, 22]. ECD and co-integration reduces the fabrication complexity, saves resources and allows integration on larger, even flexible areas for patch like structures and as part of RFID tags, which are remotely readable and preferably erasable [23].

In this paper we demonstrate the feasibility of fabricating Ag/Bi-Se memristive devices with electrochemical deposition, focusing on the characteristics such as low switching thresholds and obtaining non-volatile behaviour. We first present the microfabrication of SU-8 polymer templates and follow up with ECD of Bi_xSe_y with potentio- and galvanodynamic methods for depositing thick embedded memristive pillars. The fabrication is followed by material characterization and electrical characterization of the memristive transport properties. The constraints by the envisioned co-integration are applied and evaluated for use in combined systems.

2. Experimental

The devices were fabricated using a bottom-up approach by growing Bi_xSe_y with electrochemical deposition (ECD) from a liquid electrolyte solution. In order to confine the growth to specific locations and dimensions, molds were fabricated using microfabrication techniques shown in figure 2(a). The dies were made by first applying a photoresist lift-off technique (AZ1505, LOR5B) to pattern the four separate bottom metal contacts onto a Si wafer with a 2 μm thermally oxidized surface layer for preventing electrical conduction between the electrodes. A 10 nm Ti adhesion layer, followed by a 200 nm Au layer were sputtered onto the pattern and the unwanted parts were lifted-off using DMSO (TechniStrip Micro D350). The electrodes served both as a working electrode (seed layer) for ECD, as well as a common bottom contact of the memristive devices. A chemically resistant SU-8 polymer layer was deposited by spin coating, followed by UV photolithography to pattern the circular holes for material growth. The wafer was diced into 2 $\times$ 2 cm dies, containing approximately 1000 holes of different diameters, ranging from 10 to 500 μm. This way, templates of different aspect ratios and dimensions were fabricated, with (SU-8) thicknesses of 10, 20 or 30 μm. A common problem with electrodepositing into microstructures is to only expose the metal seed layer inside the molds and prevent liquid penetration and ECD from occurring at the connections to the instruments. This would faster deplete the electrolyte, add additional resistance to the setup and change the charge transfer and applied voltage during the deposition. To this end, a custom PTFE die holder was designed to electrically connect and hold the microfabricated dies in place with copper clips, while two concentric Viton O-rings were used to only expose the micromolds to the electrolyte (figure 2(b)) and prevent leaks of the nitric acid based solution.

Bismuth selenide was electrochemically deposited with a three electrode setup from an aqueous nitric acid based solution (0.5 or 1 M), containing equimolar concentrations (1.5, 3 or 6 mM) of bismuth nitrate pentahydrate $Bi(NO_3)_3{\cdot}5H_2O$ and selenium dioxide SeO_2. The die was connected as a working electrode and a Pt coated Ti plate was used as a counter electrode to close the circuit. An Ag/AgCl double junction reference electrode was used for potential monitoring with a Metrohm Autolab PGSTAT302 responsible for supplying voltages or currents. Prior to deposition, the solution was ultrasonicated and deaerated with N_2 gas to eliminate bubbles trapped in the template holes. The pH was adjusted to around 1 by dropping concentrated nitric acid into the solution, which was heated in a water bath to 40 °C and stirred with a PTFE coated magnet throughout the deposition.

While ECD offers the advantages of deposition into micromolds, the parameters have to be carefully adjusted to the geometries to yield the desired material properties. In order to test the flexibility of the method and accommodate the thicker thermoelectric device requirements, several electroplating methods have been explored. We start with the cyclovoltammetric (CV) investigations of the electrochemical

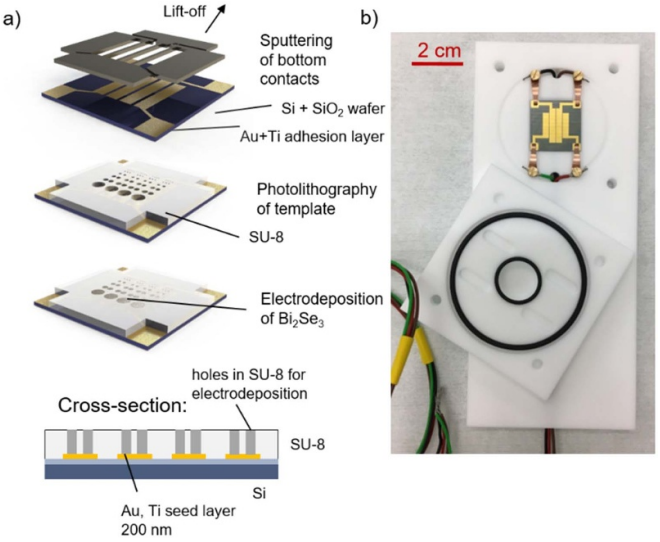

Figure 2. Fabrication of microtemplates. (a) Microfabrication of dies for the templated electrodeposition process. (b) Die clamped in a custom PTFE holder for ECD.

potentials at which reduction and oxidation occur. We evaluate the use of constant vs. pulsed potentiodynamic deposition methods and explore how different deposition cycle timing affects the growth. The requirement of thicker films can introduce a progressive increase of resistance from the already deposited material and change the growth as the size increases. To mitigate this by better controlling the number of electrons involved in the reaction, an approach of galvanodynamic deposition was investigated and evaluated with EDX.

In order to understand the reactions taking place at the working electrode, CV sweeps from -0.8 to 0.8 V (vs. reference electrode) with a rate of 100 mV s^{-1} were measured. Singular depositions of either Bi or Se on a Au coated Si die were performed from 1 M HNO_3 aqueous solutions containing 6 mM $Bi(NO_3)_3{\cdot}5H_2O$ or 6 mM SeO_2, respectively. For cyclic voltammetry of Se on Bi (figure 3(b)), Bi was first deposited at a constant voltage of -0.05 V for 20 min on a Au coated die. Similarly, Se was deposited at -0.35 V for 20 min. As seen in figure 3(a) for the deposition of Bi on Au, the reduction occurs in the negative voltage range with a significant peak at -0.06 V (labelled 'I'), attributed to the reduction of Bi:

$$Bi^{3+} + 3e^- \rightarrow Bi^0. \quad (1)$$

The broad peak in the anodic scan with a maximum around 0.1 V ('II') represents bismuth oxidation back to Bi^{3+}, whereas the small peaks at 0.17 and 0.24 V ('III') result from deposition and stripping of a Bi monolayer [24].

Further negative voltages below -0.7 V in all sweeps cause hydrogen evolution:

$$2H^+ + 2e^- \rightarrow H_2. \quad (2)$$

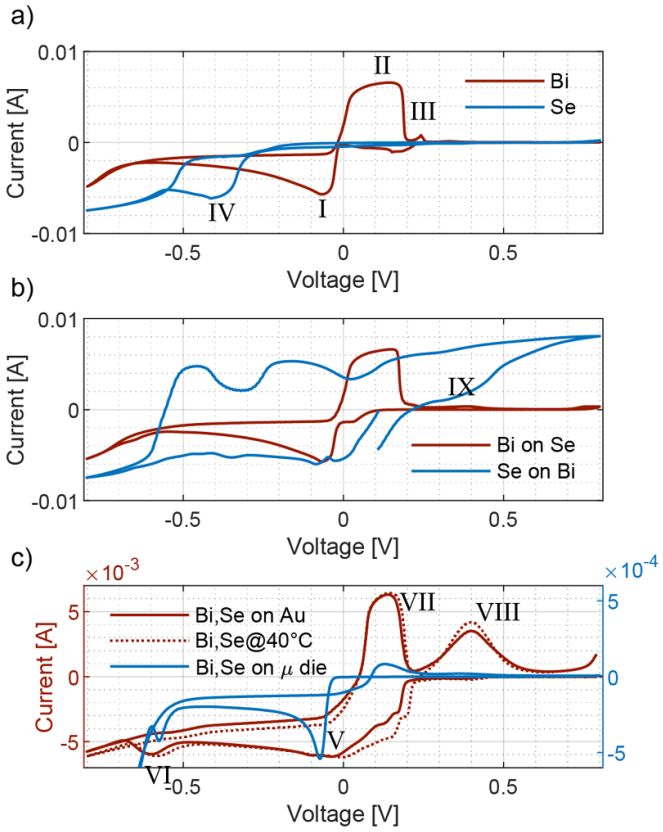

Figure 3. Cyclic voltammetry of Bi, Se on Au (top) and combined Bi, Se solutions (bottom) on an Au sputtered electrode vs a 20 μm thick micro template. The middle graph shows CV sweeps of Bi on previously deposited Se and Se redox sweeps on previously deposited Bi.

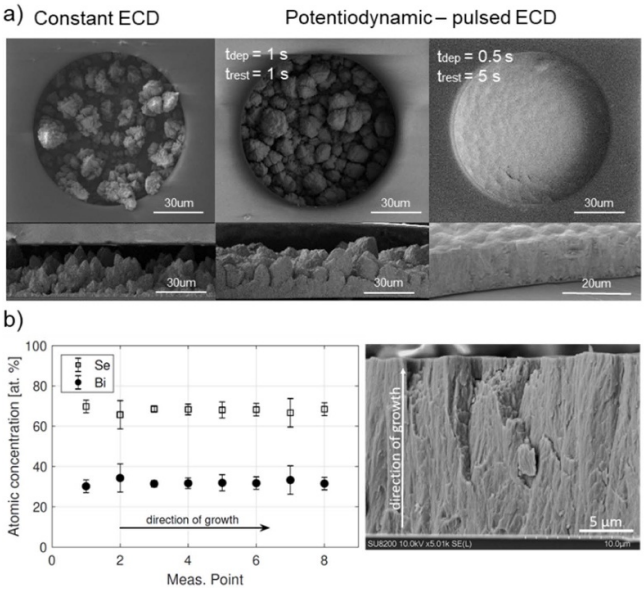

Figure 4. Electrodeposition into molds. (a) Top views and cross-sections of constant deposition at 0 V_{DEP}, vs. adjusted potentiodynamic deposition at 0 V_{DEP}, 0.2 V_{REST}. (b) EDX atomic concentration measurements along 12 μm of the cross-section from a 0 V_{DEP}/0.5 s, 0.2 V_{REST}/5 s deposition.

Depositing Se on Au (figure 3(a)) can be described by the reaction:

$$Se^{4+} + 4e^- \rightarrow Se^0, \tag{3}$$

with a peak occurring at −0.41 V ('IV') where most reduction occurs. At lower potentials, solid deposited Se is further reduced to soluble Se^{2-} [24].

The co-deposition from a 6 mM $Bi(NO_3)_3{\cdot}5H_2O$ and 6 mM SeO_2 1 M HNO_3 solution is shown in figure 3(c). A broad cathodic peak around −0.04 V ('V') is attributed to the reduction of Bi_2Se_3, whereas negative potentials around −0.6 V ('VI') further reduce the electrodeposited selenium to selenide.

$$3Se^{4+} + 2Bi^{3+} + 18e^- \rightarrow Bi_2Se_3\,(s), \tag{4}$$

$$Se\,(s) + 2e^- \rightarrow Se^{2-}. \tag{5}$$

The anodic scan direction shows oxidation of Bi to B^{3+} at 0.1 V ('VII'), as seen in the Bi-only CV sweep. An additional peak appears at 0.4 V ('VIII') where Bi_2Se_3 is oxidized to Bi^{3+} and Se^{4+}, also visible in the scan of Bi on a Se substrate (figure 3(b), 'IX'). At higher potentials around 0.8 V, the free Se oxidizes to Se^{4+}. The sweep of Se on pre-deposited Bi (figure 3(b)) shows an opening in the CV sweep, likely due to the additional stripping of Bi at positive voltages. When the voltages return towards zero, the reduction of Se is also occurring on the stripped locations with the exposed gold substrate that shifts the peak locations and causes the discontinuity. With CV sweeps performed on microtemplates, the diffusion limited transport of reactants to the deposition sites and a smaller area exposed to the electrolyte result in a smaller current and a slight shift of the redox peaks (figure 3(c)).

Based on the CV experiments, we deduced that a voltage window from −0.4 to 0.2 V was appropriate for material growth by Bi_2Se_3 reduction. At lower negative deposition potentials, the deposits did not form a compact structure (see S.I., figure 1) whereas high positive potentials yielded no deposition. Experimentally it was determined that instead of applying a fixed reduction potential for deposition, a pulsed voltage signal alternating between a depositing potential and a resting potential yielded more dense and smooth structures. During the deposition time the reduction of ions from the solution occurs at the seed layer and continues to fill the mold bottom-up. A resting potential, where according to the CV sweep, no oxidation or reduction occurs allows for the side products of the deposition to diffuse away and new reactants to reach the deposition sites. A comparison of differently timed depositions performed at the same 0 V_{DEP} and 0.2 V_{REST} potentials (vs. reference electrode) can be seen in figure 4(a). Depositing at 0 V_{DEP} for 0.5 s with a resting potential at 0.2 V_{REST} for 5 s yielded the best results in terms of film compactness (figure 4(a), right), whereas a longer pulsed deposition time of 1 s resulted in more dendritic growth (figure 4(a), middle). With geometrical variations of microtemplates, a CV sweep was performed prior to the start of the deposition to accurately tune the potentials around 0.2 and 0 V. An EDX

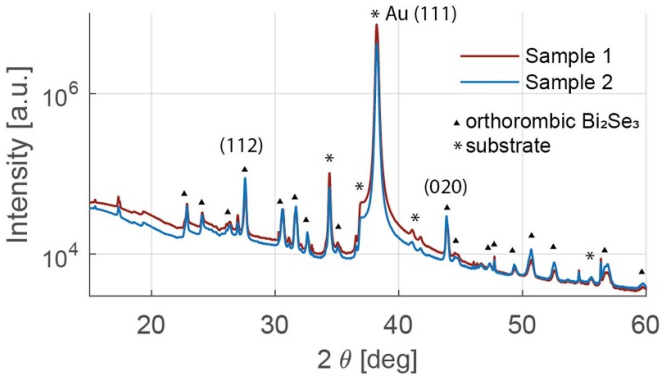

Figure 5. X-ray diffraction of electrodeposited Bi_2Se_3 films show the presence of an orthorhombic crystal structure (here shown for two samples deposited at the same conditions). An XRD scan of the substrate is included in the S.I.

scan for eight vertical positions along a broken-off cross-section of such a deposit at six different horizontal locations (error bars) shows a Se-rich uniform composition throughout the thickness of the devices (figure 4(b)). The growth rate of the templated deposits with the above mentioned parameters was roughly 1 μm per hour and left until the deposits slightly overgrew out of the templates.

To further investigate the crystallinity and structural properties, x-ray diffraction measurements were performed. Given that the spot size of the XRD was too large to adequately analyse the material embedded in the microtemplates, a deposition of thin-films was performed on Au sputtered Si dies for the XRD scans seen in figure 5. The XRD scans of two samples deposited with the same conditions 0 V_{DEP}/0.2 V_{REST}, 0.5 s t_{DEP}/5 s t_{REST} for 7.6 h exhibit pronounced peaks in the (112) and (020) directions and match an orthorhombic Bi_2Se_3 structure as found in literature [25]. No additional pronounced peaks are displayed, indicating that the excess Se observed from the EDX measurements is likely in interstitial positions without additional agglomeration that would be pronounced in the x-ray diffraction.

Similarly to the potentiodynamic deposition, a resting period of 5 s where the current remains zero $I_{REST} = 0$ was applied with the galvanodynamic method. During the deposition pulses of 0.5 s, a constant current value was chosen. Figure 6 presents the resulting deposits grown at different deposition current values, that show a decrease in selenium content with increasing current. A deposition current density of around 80 A m^{-2} corresponds to 3:7 Bi:Se ratio displayed with the potentiodynamically deposited pillars at 0 V in figure 4(b). Along with increasing surface roughness, the deposits grow at a faster rate with higher deposition currents.

The depositions used for further fabrication of memristive devices were overgrown and manually polished using a grit 4000 SiC paper to make the deposits level with the SU-8, which allowed subsequent deposition of the top contacts. After Ar ion surface cleaning, 150 nm of Ag was evaporated through a shadow mask on top of the deposited structures, so that the top electrode covered the whole surface of each deposit. A Signatone probestation was used to contact the bottom layer (common to all devices on one electrode) and a top Ag contact of each device. Keithley 2400 SourceMeter was used to acquire current–voltage characteristics and source pulses, while a Temptronic TP03210 chuck, Tektronix AFG310 function generator and R&S RTB2004 oscilloscope with a transimpedance amplifier DLPCA-200 were used to perform temperature dependent measurements and scaling tests in figures 10–12. The characterization included in this paper presents measurements of multiple devices from different fabrication runs (a detailed table listing the devices is included in the supplementary information). The reported behaviour was repeatedly observed in our devices, however at this point a statistical analysis has not been not performed.

3. Results

The current–voltage curve in figure 7 shows a typical bipolar memristive pinched hysteresis comprising two distinct low resistance (R_{LRS}) and high resistance (R_{HRS}) slopes, ranging around 7.6 kOhm and 1 MOhm for a 30 μm thick device with a 75 μm diameter, deposited with the potentiodynamic method. Starting from 0 V, as the voltage increases in the positive direction (+ on the Ag top contact), the current experiences a drop in magnitude at around 0.1 V, leading to a higher resistance of the device. Applying a sufficient voltage of the opposite polarity results in a transition from high resistance back to the initial low resistance state. The devices exhibit low switching thresholds around 100 mV for both polarities and display non-volatile behaviour, meaning that the resistance stays in the same state when the external voltages are removed. As seen in the inset of figure 7 and discussed later, no memristive effect was observed when using Au as both the top and bottom electrodes.

Both SET and RESET processes for the same device shown in figure 7 are replotted in a *log-log* plot in figure 8. The slope values around 1 indicate an ohmic transport regime at low voltage regions with both polarities. In the non-linear regime, a number of conduction mechanisms have been previously discussed in memristive devices and can be either electrode-limited (Schottky emission, Fowler-Nordheim or direct tunnelling, Thermionic-field emission) or bulk-limited (Poole-Frenkel emission, Space-charge-limited conduction, hopping, ionic or grain boundary limited conduction) [26]. To discern between the different mechanisms, we here examine the I–V characteristics in more detail.

Looking closely at the negative portion of the IV sweep (figure 8), four separate regions can be distinguished, typical for trap governed and space-charge limited conduction regime [26, 27]. At low voltage levels, the current is linearly proportional to the voltage through Ohm's law $I \propto V$ and thermally generated charge carriers govern the transport. As the voltage increases, the injected charge carriers start prevailing over the thermally generated electrons and dominate the conduction, resulting in a square-law region $I \propto V^2$. Upon further voltage increase, the traps in the interface region get filled by injected electrons and display a high current $I \propto V^{11}$. Once all traps are filled, the trapped electrons start repelling the injected

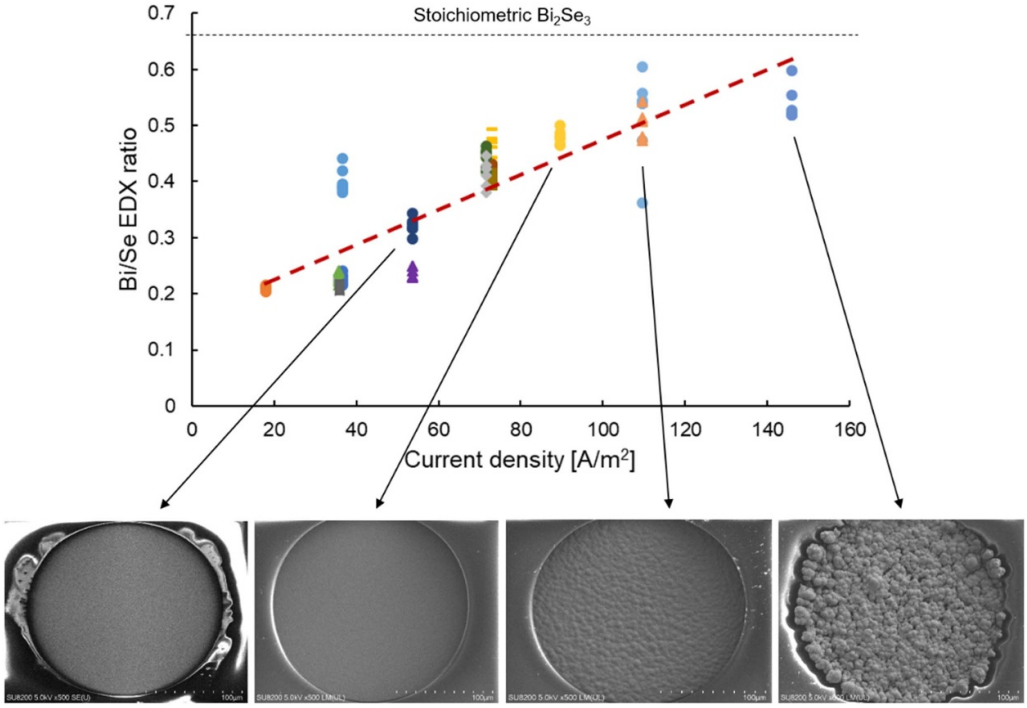

Figure 6. Deposition current density vs. Bi/Se content ratio. EDX Bi:Se ratio of samples deposited at different deposition current densities. The same coloured symbols designate different micromold pillars on the same die. The bottom row shows top view SEM images of 200 μm diameter deposits from the corresponding samples.

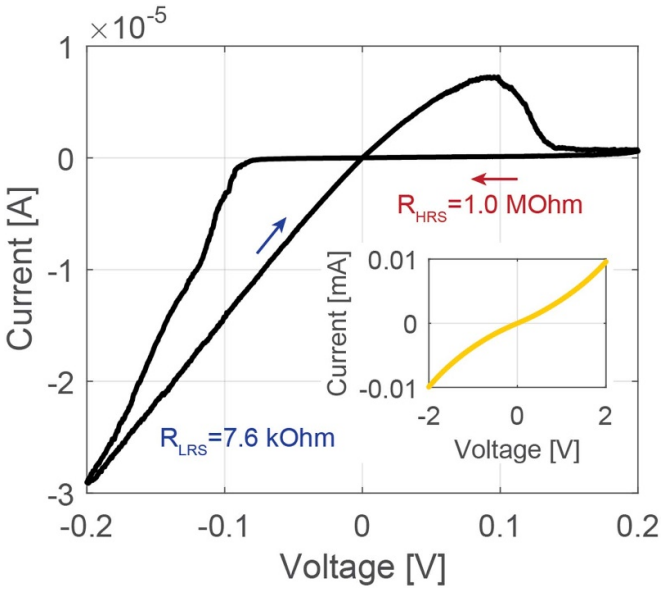

Figure 7. Current–voltage pinched hysteresis. IV characteristic displaying a clear memristive pinched hysteresis for a 30 μm thick 75 μm diameter device. The inset shows an IV sweep with no hysteresis for both top and bottom Au electrodes.

charges and the current–voltage relation returns to the square law $I \propto V^2$, known as space charge limited current. Trap filling and space-charge-limited bulk conduction effects are therefore observed in the negative voltage sweep.

In the positive sweep direction, the same curves were replotted as $\ln(I)$ vs. $\sqrt{V}$ and $\ln(I/V)$ vs. $\sqrt{V}$ to determine whether the devices exhibit Schottky or Poole–Frenkel behaviour (figure 9). The linearity shows that the observed transport is closer to the electrode-limited Schottky type behaviour, following the typical emission regime:

$$J = AT^2 e^{\frac{-q\left(\phi - \sqrt{qE/4\pi\varepsilon_r\varepsilon_0}\right)}{kT}}, \qquad (6)$$

where A is the Richardson constant, ϕ the barrier height, T temperature and J the current density.

Temperature dependent measurements in figure 10 show that the HRS to LRS voltage threshold under negative bias displays no significant change, with no energy barrier comparable to kT. The LRS to HRS transition voltage threshold, however, shows temperature dependency and shifts to lower values with increasing temperature.

Bi_xSe_y displays a small bandgap lower than 0.3 eV for rhombohedral Bi_2Se_3 [28], smallest indirect gap 42 meV for BiSe [29] and 0.9 eV for orthorhombic Bi_2Se_3 [25]. The contact region may contain a number of phases with the distribution of band gaps (0.02–0.2 eV, 0.6 V for Ag_2Se and $AgBiSe_2$ [30, 31]) and very similar work functions (4.3 eV silver, Bi 4.25 eV [32], Ag_2Se of 4.3 eV [33]). This results in complex electrochemistry at the contact, which overall gives the desirable properties for the observed memristive behaviour. However, due to lack of methods that would allow observation of ionic transport in unmodified memristive devices

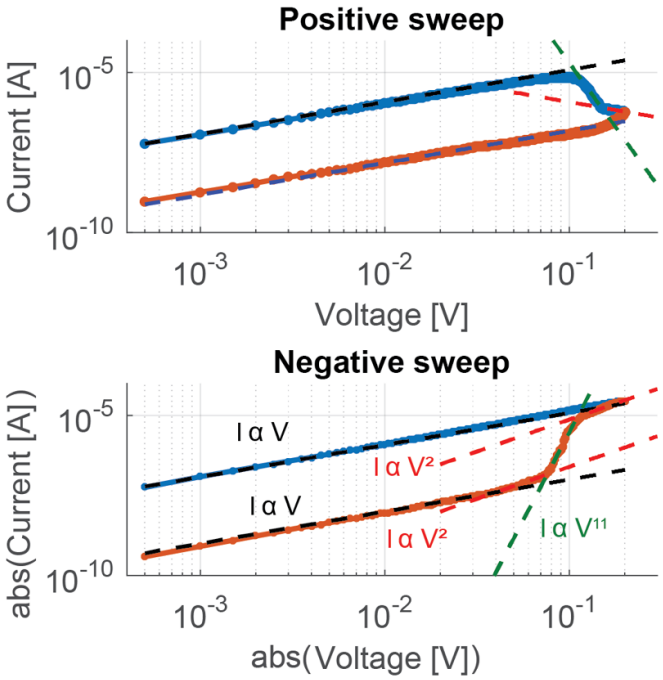

Figure 8. Conduction regions log-log scale plots of positive and negative sweep segments exhibit ohmic conduction at low voltages and nonlinearities at higher voltage values.

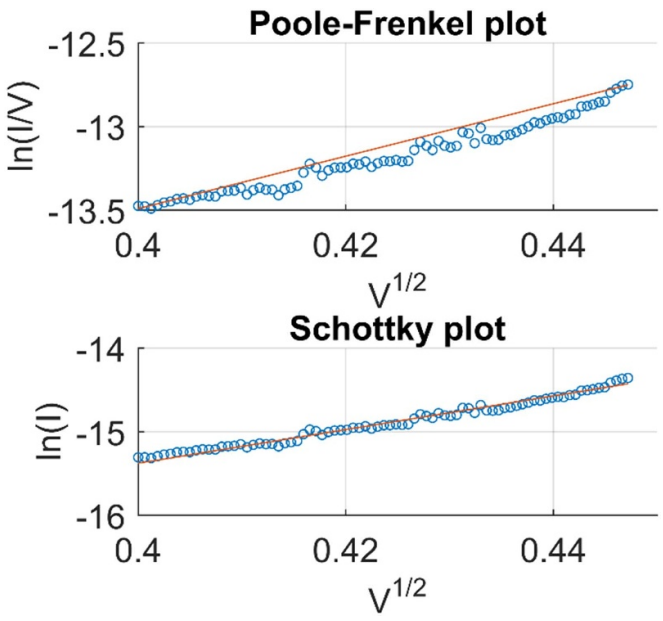

Figure 9. Poole–Frenkel and Schottky plots. Non-linear portion of the HRS in the positive sweep plotted in a Poole–Frenkel plot and Schottky plot. Blue dots indicate the experimental data while the red line shows a linear expected slope in each regime.

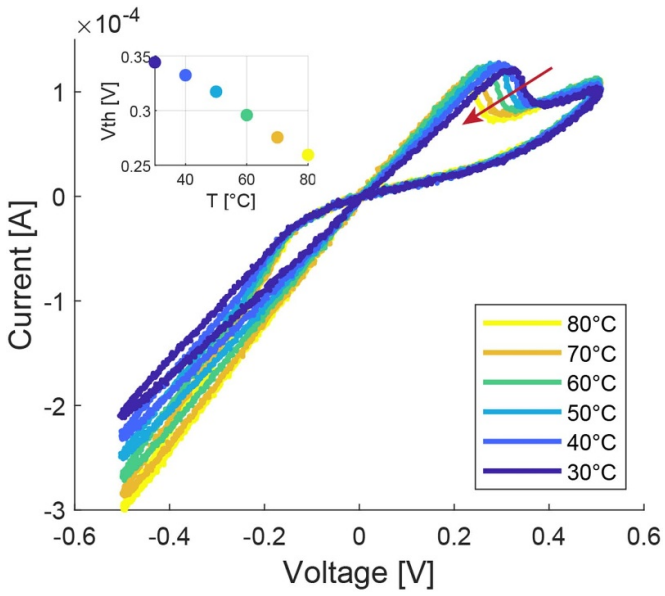

Figure 10. Temperature dependence. Voltage threshold lowering with temperature in the positive sweep direction and insensitivity of the HRS to LRS transition threshold. The inset shows points taken at the LRS to HRS transition at different temperatures, as indicated by the red arrow.

[34] it is difficult to discern the dominant switching mechanism that can often appear as a combination of several effects. The resistance changes are a result of redox reactions taking place in the memristive materials and can be caused by voltage or local current-induced temperature. Electrochemical metallization mechanisms (ECM) involve dendritic growth of active electrode materials such as Ag to bridge the two electrodes and form conductive paths. In transition metal oxides, thermochemical mechanisms cause the formation of conductive filaments through thermal breakdown of oxides bridging the two electrodes. Valence-change mechanisms can occur in filamentary switching or at a localized area around the electrode interface [35]. This type of memristive behaviour was previously shown in sputtered and sublimated Bi_xSe_y by Tulina *et al* [18, 36] and explained by redistribution of Se ions which move under electrodiffusion at sufficiently high electric fields. At the local region around the silver contact, Bi_xSe_y forms selenium vacancies which exhibit low formation energy and act as electron donors. Anti-site defects, grain boundaries and impurities result in increased electrical conductivity around the top electrode. When a positive voltage is applied on the Ag electrode, selenium anions from bulk start to migrate towards the electrode interface region, filling the vacancies and thereby changing the resistance around the interface to a high value. Applying a negative voltage (− on the top Ag electrode) causes the Se anions electromigrate back to the bulk leaving vacancies near the interface region, resulting in R_{LRS} [18].

No forming voltage was required to obtain the hysteretic behaviour, as typical for interface-type memristors. According to Pan *et al* [37], the low resistance state should be inversely proportional to the memristor device area with interface-type switching behaviour. Therefore the interface-type behaviour with local redistribution of dopants was verified by performing scaling tests (figure 11) with 50, 100 and 200 μm diameter devices and shows the inverse relation between the electrode area and R_{LRS}. In a filament-type memristive device where the local switching is caused by the formation of filaments, scaling has a less pronounced effect on the resistance [9]. It

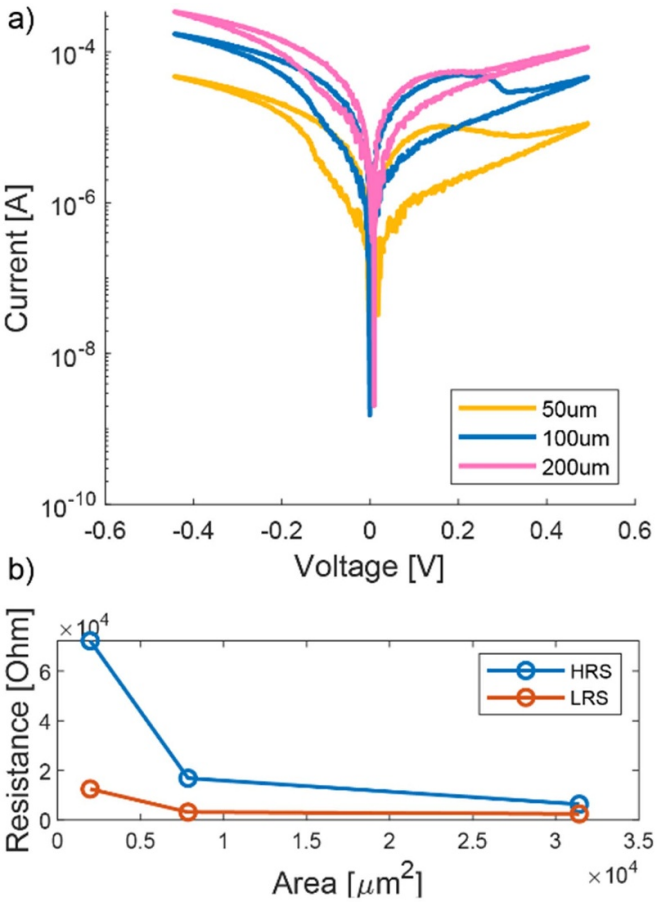

Figure 11. Device diameter scaling. Scaling tests for 20 μm thick devices show that the R_{LRS} is inversely proportional to the device area (b), indicating interface-type memristive behaviour. The sweeps in (a) are the averages of 18 different memristors at each diameter size.

should be noted that the diffusion of reactants can vary when electrodepositing materials in holes with different diameters on the same die and can result in some variation of the deposits. This can in turn affect the memristor IV sweep comparison between the differently sized diameters in figure 11.

To verify the role of silver on the memristive effect of our devices, a gold top electrode was evaporated to form a Au/Bi_xSe_y/Au device. In contrast to Ag electrodes, our measurements with gold electrodes showed no memristive behaviour, even at higher voltage sweeps of ± 2 V (figure 7 inset). According to Takagaki *et al*, material incorporation does not occur when Au is used to grow Bi_2Se_3 films [38, 39], also confirmed by Walsh *et al* with Au evaporation on Bi_2Se_3 films [40]. The resistance of the as-deposited films with Au contacts typically ranged from a few hundred ohms to a few kilo ohms—lower or comparable to the LRS of Ag/BiSe devices. In contrast to Au, previous publications have shown different types of diffusion of Ag into Bi_2Se_3 crystals in the forms of intercalation, Ag^+ solid solution or new phase formation. Long range disorder in chalcogenide-based memristive devices results in high mobility of metal ions from the typically used active electrodes such as Ag and Cu [18, 35, 41, 42]. Intercalation of Ag in Bi_2Se_3 layers has been observed, where the metal ions are placed between the quintuple layers connected by Van der Waals forces [43]. Such intercalation however only occurs with very low Ag atom concentrations [44] and precipitate nucleation is more likely when more atoms are involved. Ag can appear in a substitutional arrangement, partially replacing Bi atoms to form $Ag_xBi_{2-x}Se_{3\pm\delta}$ compounds and cause Se excess or deficiencies [45] that play a dopant role in the resistance changes of our devices. Substitution was also reported by Ferfolja *et al* who have experimentally shown how Ag nanoparticles deposited on single crystal Bi_2Se_3 agglomerate and change morphology after 3 d of exposure at room temperature [46]. After 70 d on the surface, they completely disappear due to diffusion into Bi_2Se_3 and new phase formation. Their XRD scans show that a mixture of Bi_2Se_3 plates and Ag particles forms new phases of $AgBiSe_2$ and Ag_2Se, while diffraction lines of metallic Ag were no longer visible. The following solid-state reaction was proposed to describe this process:

$$3Ag + Bi_2Se_3 \rightarrow AgBiSe_2 + Ag_2Se + Bi. \qquad (7)$$

In their study, they did not observe any intercalation that would expand the unit cell and change the position of the x-ray diffraction lines for Bi_2Se_3. From this we conclude that the diffusion of Ag plays a crucial role in the memristive transport.

Since the distance between our electrodes is large in the range of tens of microns, it is unlikely that a conducting Ag^+ filament would occur connecting the top and bottom electrodes as observed in ECM devices. However this does not exclude the possibility of short filamentary path formation between diffused Ag in the interface region, leading to a lower overall device resistance. A comparison between the averaged measured currents of 10 different hysteresis displaying memristors for 10, 20 and 30 μm thicknesses is shown in figure 12(a). As the device thickness increases, the overall resistance is increased and the additional material acts as a bias resistance (R_B) in series to the interface region R_I where the resistive switching is taking place. While the overall current decreases with the device thickness, the added bias resistance causes the switching thresholds to slightly shift to higher values with thicker devices. This is more apparent in the LRS to HRS (RESET) transition, where the added resistance R_B is closer to the ranges of the R_{LRS} and the voltage drop across the memristor interface changes more significantly with different thickness. The changes in the HRS to LRS transition (negative voltages) are lower since the voltage across the switching interface is closer to the applied overall voltage because of $R_{HRS} \gg R_B$. In a filamentary device where a conductive channel bridges the two electrodes, the RESET voltage does not significantly change with increasing thickness, since the Joule heating involved in the filament rupture is less affected by the length changes [47].

Similarly, when comparing memristors with different selenium content (figure 12(b)), the Se-richer devices display a higher resistance value and result in a shift of the voltage thresholds to higher voltages.

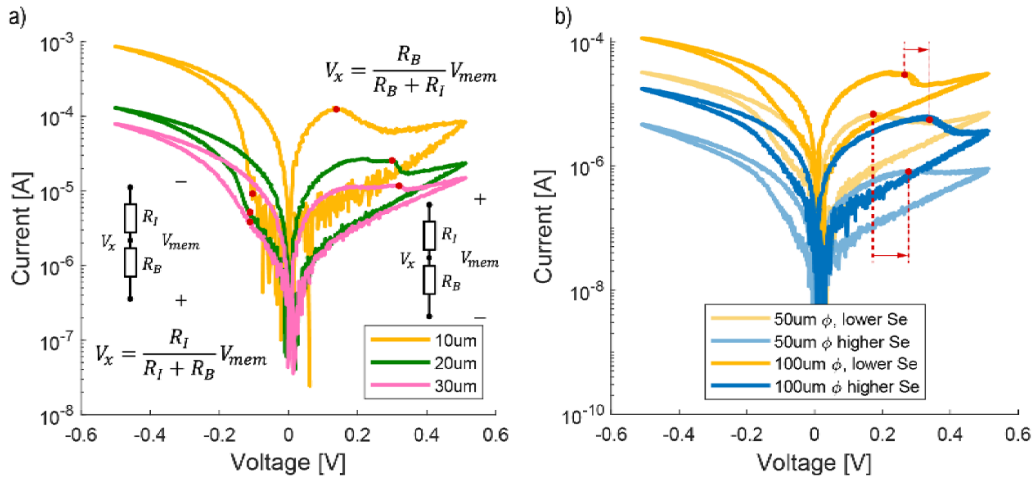

Figure 12. Device thickness and Se content comparisons. (a) Mean IV sweeps of ten (100 μm diameter) memristors at three different substrate thicknesses. The red points indicate the approximate threshold voltages. (b) A comparison between the mean IV sweeps of 50 and 100 μm diameter memristors with different selenium content (deposited at 90 and 300 A m^{-2}). Red arrows show the shift in the switching thresholds.

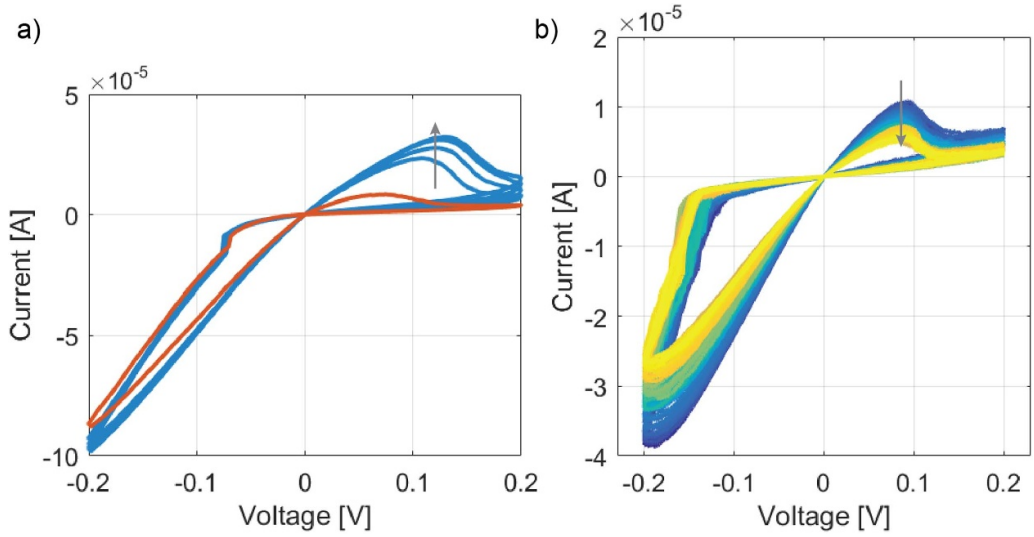

Figure 13. Current changes with repeated IV sweeps. (a) The first sweep measured in a pristine device after fabrication is highlighted in red. (b) 100 sweeps on a previously characterized device (the first sweep is coloured dark blue while yellow shows the 100th sweep).

While no forming voltage step was required to acquire the hysteretic behaviour, we have however observed that the first sweep in a new device starts with a resistance higher than the R_{LRS} (figure 13(a)). In accordance with the discussion, this initial resistance points to new phase formation already upon Ag contacting. Further application of a positive potential on the Ag electrode increases the resistance to R_{HRS} with the first positive sweep, meaning that the Schottky barrier increases. As speculated by Tulina *et al* [18], this non-volatile resistance change is likely due to electromigration of Se precipitates drawn towards the vacancies left upon Ag atom substitution after contacting.

The repeatability of the hysteretic behaviour in 100 cycles of IV curves in figure 13(b) indicates that ionic transport likely favours electromigration through already established paths along grain boundaries and impurities. However, drift to lower currents has been observed in some devices that have been previously characterized. At this point, the current drift is not completely clear. The increase of current in pristine devices could be attributed to preferred microscopic path formation with electrodiffusion, while lowering current could be caused by device fatigue and dopant diffusion through local heating.

Based on the established literature and the present data we conclude that both Se and Ag as well as combined newly formed phases are involved in the switching process. The non-trivial behaviour, complex switching process and the promising memristive properties make the topic stimulating for further research towards clarifying the different mechanisms.

To further test the memristive operation, a series of square programming pulses were applied. 'RESET' (500 mV, 20 ms) and 'SET' (−500 mV, 20 ms) voltage pulses were each followed by a 'Read' pulse (50 mV, 500 ms) to readout the

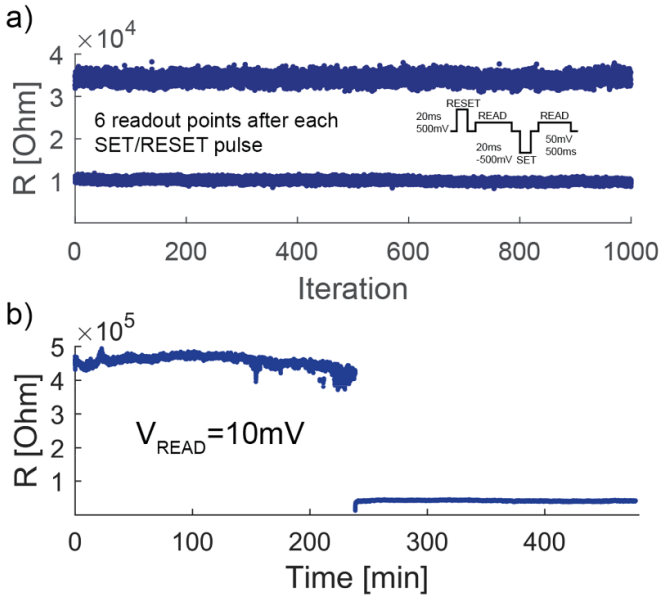

Figure 14. Repeatability and retention. (a) The inset shows one iteration of 'set', 'reset' and 'read' pulses applied to the memristor, which changes resistance after each pulse for a 200 μm diameter, 30 μm thick device. (b) Longer 4 h retention in each state after applying 500 mV RESET and −500 mV SET pulses to a 30 μm thick, 200 μm diameter device.

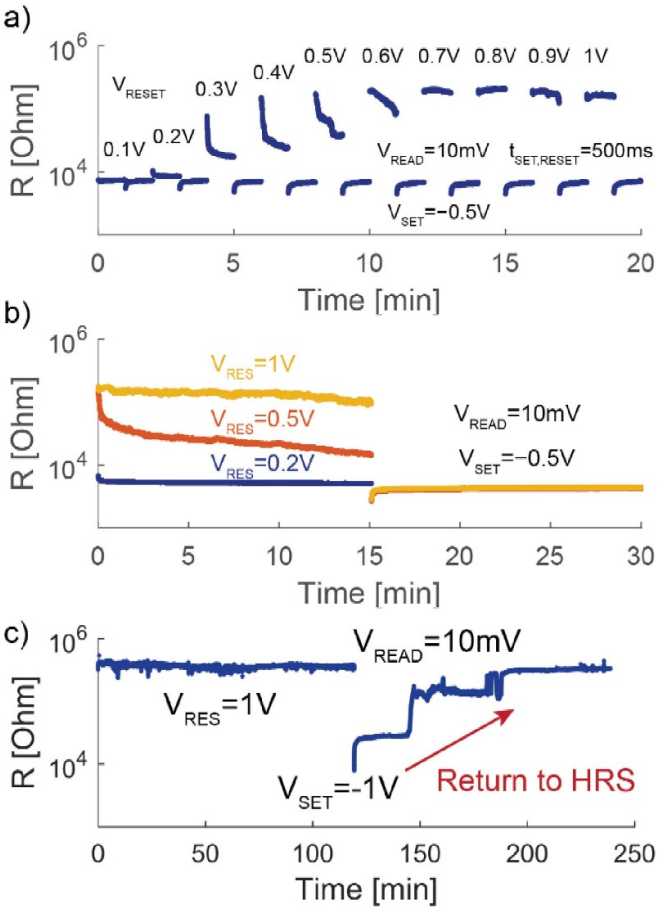

Figure 15. State stability. (a) State stability variation, depending on the applied reset voltage. (b) 15 min stability monitoring with different reset voltages. Vertical axes are in log scale. (c) 2 h monitoring of pulses after reset and set processes, where the resistance (log scale) returns to a higher value over time.

resistance of the memristor. As seen in figure 14(a) for 1000 iterations (1 iteration equals a sequence of RESET, READ, SET, READ pulses with a total duration of 1040 ms), with each reset or set pulse applied, the resistance changed value by around 25 kOhm.

The non-volatile retention of resistance in an 4 h measurement (in each state) is shown in figure 14(b), where a 500 mV RESET (at 0 min) and a −500 mV SET pulse (at 240 min) were used to switch the resistance while a continuous readout bias of 10 mV was applied. The low resistance state displays greater stability, while fluctuations in the high resistance can be attributed to both a low readout current noise, as well as resistance fluctuations from ion drift in the active layers.

Resistive switching devices often display multiple states which might exhibit different retention times and relaxation to more stable states [48]. This can be seen in figure 15(b) where different amplitudes of RESET switching voltages lead to resistance states with decaying values in a 15 min measurement with a 10 mV continuous readout voltage. Similarly, figure 15(a) shows how supplying RESET pulses with increasing amplitudes bring the resistance to different levels. A higher than necessary SET voltage of −0.5 V was applied between each RESET, to ensure that the memristors were in the lowest possible state. Switching with a low reset voltage results in a low R_{HRS} to R_{LRS} ratio, while states obtained with a reset voltage around 0.4 V decay faster. Higher amplitude reset pulses lead to better resistance stability that does not rapidly decay towards lower values. An opposite direction drift is shown in figure 15(c) for a 4 h measurement of the same device as in figure 14(b). After the switching to a LRS, the memristance starts to rise and ends up returning to the HRS around 350 kOhm. The choice of switching pulses, as well as the history of applied signals should therefore be carefully considered when programming the resistive switching devices.

4. Discussion

Both presented potentiodynamic and galvanodynamic methods result in thick films displaying clear memristive behaviour when combined with Ag electrodes. Galvanodynamic deposition offers greater tuning control over the selenium content of the memristors (figure 6), that affects the resistance of the devices (figure 12(b)) and their thresholds. Comparing to the previously measured sputtered or sublimated Bi_2Se_3 memristors [19], our electrodeposited devices show a greater overall resistance in both LRS and HRS due to larger device thickness and an orthorhombic crystal structure with a larger expected band gap. Tulina *et al* reported $R_{LRS} \sim 41$ Ohm and $R_{HRS} \sim 840$ Ohm with a rhombohedral structure and different device sizes. The HRS/LRS ratio (∼100) is greater with our electrodeposited memristors, likely owing to more grain boundaries and defects that are involved with the ionic transport. The switching thresholds of the devices display similar

voltages around 100 mV that are sufficiently low for the proposed hybrid application in combination with thermoelectric sensors. With thicker and more Se-rich devices (figure 12), the thresholds shift to higher values by a few millivolts due to the added bias resistance of the material not involved in the switching mechanism. In contrast to that, a lowering of the voltage thresholds in the RESET direction was observed with the measurement of IV sweeps obtained at elevated temperatures (figure 10), which also has to be considered in the co-integration with a thermoelectric device.

As opposed to computing and memory applications where fast switching speeds are highly desirable, the envisioned application does not require the memristors to react to fast changes of the applied voltage, since these are limited in speed by the heat-flux transfer through the thermoelectric material. The displayed interface-type memristors are typically slower than filamentary switching, likely due to the lack of associated Joule heating that elevates the temperature and increases ion motion involved in the switching [34].

The retention measurement (figure 14(b)) displays the non-volatility, necessary for the envisioned application, however as seen in figure 15(a), applying increasing amplitudes of switching voltages leads to different resistance states with varying stability over time. This is also visible in the concept of combined memristive-thermoelectric system in figure 1 where the initial resistance value decays over time. An observed climb of resistance to the opposite HRS direction in figure 15(c) shows that drift can occur in both directions. Given that the presented memristors are non-encapsulated devices with exposed Ag top contacts prone to oxidation, this drift and state stability are likely affected by moisture and air exposure. Kong *et al* [49] have shown that ambient conditions introduce native oxide/hydroxide growth and local doping at the surface of Bi_2Se_3. BiO_x as well as SeO_x presence in 2 d air exposed samples has been observed with XPS measurements, as well as excessive Se that tends to gradually precipitate since a 'Se deficient state is more thermodynamically favourable under ambient conditions' [49]. This surface depletion of selenium, leading to n-type doping by Se vacancy formation was also reported to result in a 1.4 eV decrease in work function [50] and goes in hand with the Se deficiency at the top electrodes reported by Tulina *et al* [18]. H_2O molecular adsorption without additional reactions taking place has been shown to act as an electron donor in chalcogenides [51] which could, along with moisture absorption of SU-8 photoresist [52], affect the long term stability of the devices. The effects of increased air and humidity exposure between processing steps on the characteristics of the memristive devices need to be further investigated.

Furthermore, the topology of electrical contacts has a considerable effect on the electrical field geometry, and influences the local formation of percolation paths for current in the memristive material [17]. Microscopic imperfections in the top electrode due to polishing scratches and any porosity of the electrodeposited materials mean that the electric field applied on the macroscopic sized electrodes forms highly localized electrical fields that along with inhomogeneous impurities and surface doping form for a complex system where a quantitative approach and direct observation are not possible. Therefore the addition of a passivation step and integration of the memristors in a final device are also expected to improve the demonstrated performance. An additional factor that has to be considered in the comparison of memristors is that as the material growth approaches the openings of the micromolds, the deposition becomes less diffusion-limited and can result in a different growth regime. This is also in the comparison of diameters, since the different diameters on a common die deposited in the same ECD step can display slightly different deposition rates that can result in increased roughness. The variation Se content also changes the device roughness that affects the overall topology and introduces more grain boundaries. The ECD growth conditions can be further optimized for a specific geometry of the devices in a final combined device.

5. Conclusions and outlook

Here we demonstrate that the room temperature thermoelectric material bismuth selenide exhibits memristive properties that can be used for functional co-integration in hybrid 'zero-power' sensors for autonomous applications. We present that bismuth selenide in combination with Ag exhibits memristive effects when deposited with the fabrication method of electrochemical deposition. Applying resting and deposition cycles for the electrochemical growth results in compact thick films that can be used for memristive devices as well as offer future possibilities of combining process flows for thermoelectric sensors. Local Se doping redistribution, enabled by new phase formation due to diffusion of the active Ag electrode is likely the cause of memristive behaviour in our devices. Schottky and space-charge limited mechanisms fit with the measured data acquired by IV sweeps, while retention and pulsed measurements show non-volatile operation, with low switching thresholds. Not shown in the previous studies of resistive switching in this material combination, we also present pulsed measurements of 1000 set and reset cycles, endurance measurements and state stability.

The ECD method shows the desired compatibility with the fabrication requirements for thermoelectric devices that would allow for reduction of processing steps in the fabrication of zero power autonomous devices. ECD into molds as used in this paper could also offer the advantage of progressive doping throughout the thickness of the metal–insulator-metal memristor structure, to tailor the ionic transport between the interlayers and thereby tune the memristive behaviour (SI, figure 3). This could enable seamless integration of different active/buffer layers that can improve the switching characteristics of memristive devices [53, 54]. Additionally, for better determination of the nanostructuration and crystallinity of the grown materials that would help in understanding the memristive transport, micro XRD scans or TEM observation of the material grown inside the templates would be beneficial.

This research is continuing in the integration of the presented memristors into devices joining thermoelectric and memristive properties of bismuth selenide in a common fabrication process flow using ECD to form a novel type of 'zero power' logging sensor.

Data availability statement

Mihailovic Ian, 2021, Memristive behavior of electrodeposited bismuth selenide, ETH Zurich Research Collection, 10.3929/ethz-b-000486155.

Acknowledgments

The authors would like to acknowledge the financial contributions from the Swiss National Science Foundation (SNSF) (SNSF-Project No. 200021_178734). We would like to thank the clean room staff of the Binning Rohrer Nanotechnology Center (BRNC) at IBM Research, Rüschlikon, as well as the ETH FIRST-CLA facility at ETH Zürich for the microfabrication assistance. The authors would also like to thank Lukas Schürz, Kordian Caplazi and Florin Püntener for their experimental and electrical characterization support, Paul Baade (Institute for Electronics, ETH) for the XRD assistance, as well as Dr Cosmin Roman for the theoretical discussions.

ORCID iD

I A Mihailovic https://orcid.org/0000-0002-2438-0197

References

[1] Zhang F, Zang Y, Huang D, Di C A and Zhu D 2015 Flexible and self-powered temperature-pressure dual-parameter sensors using microstructure-frame-supported organic thermoelectric materials *Nat. Commun.* **6** 1–10
[2] Fu Y, Zhao Y, Wang P, Xing L and Xue X 2015 High response and selectivity of a Cu-ZnO nanowire nanogenerator as a self-powered/active H2S sensor *Phys. Chem. Chem. Phys.* **17** 2121–6
[3] Abunahla H, Mohammad B, Mahmoud L, Darweesh M, Alhawari M, Jaoude M A and Hitt G W 2018 MemSens: memristor-based radiation sensor *IEEE Sens. J.* **18** 3198–205
[4] Vahl A, Carstensen J, Kaps S, Lupan O, Strunskus T, Adelung R and Faupel F 2019 Concept and modelling of memsensors as two terminal devices with enhanced capabilities in neuromorphic engineering *Sci. Rep.* **9** 1–9
[5] Mercier S, Villeneuve S, Mondor M and Uysal I 2017 Time–temperature management along the food cold chain: a review of recent developments *Compr. Rev. Food Sci. Food Saf.* **16** 647–67
[6] Bohra A K *et al* 2017 Tellurium-free thermoelectrics: improved thermoelectric performance of n-type Bi2Se3 having multiscale hierarchical architecture *Energy Convers. Manage.* **145** 415–24
[7] Snyder G J and Toberer E S 2008 Complex thermoelectric materials *Nat. Mater.* **7** 105–14
[8] Xia Y *et al* 2009 Observation of a large-gap topological-insulator class with a single Dirac cone on the surface *Nat. Phys.* **5** 18
[9] Sawa A 2008 Resistive switching in transition metal oxides *Mater. Today* **11** 28–36
[10] Kvatinsky S, Belousov D, Liman S, Satat G, Wald N, Friedman E G, Kolodny A and Weiser U C 2014 MAGIC—Memristor-aided logic *IEEE Trans. Circuits Syst.* II **61** 895–9
[11] Jo S H, Chang T, Ebong I, Bhadviya B B, Mazumder P and Lu W 2010 Nanoscale memristor device as synapse in neuromorphic systems *Nano Lett.* **10** 1297–301
[12] Pershin Y V and Di Ventra M 2010 Practical approach to programmable analog circuits with memristors *IEEE Trans. Circuits Syst.* I **57** 1857–64
[13] De Liang K, Huang C H, Lai C C, Huang J S, Tsai H W, Wang Y C, Shih Y C, Chang M T, Lo S C and Chueh Y L 2014 Single CuOx nanowire memristor: forming-free resistive switching behavior *ACS Appl. Mater. Interfaces* **6** 16537–44
[14] Zoolfakar A S *et al* 2013 Engineering electrodeposited ZnO films and their memristive switching performance *Phys. Chem. Chem. Phys.* **15** 10376–84
[15] Zaffora A, Macaluso R, Habazaki H, Valov I and Santamaria M 2018 Electrochemically prepared oxides for resistive switching devices *Electrochim. Acta* **274** 103–11
[16] Rebora C, Huang R, Kissling G P, Bocquet M, De Groot K, Favre L, Grosso D, Deleruyelle D and Putero M 2019 Conductive-bridge memory cells based on a nanoporous electrodeposited GeSbTe alloy *Nanotechnology* **30** 025202
[17] Murugesan S, Kearns P and Stevenson K J 2012 Electrochemical deposition of germanium sulfide from room-temperature ionic liquids and subsequent ag doping in an aqueous solution *Langmuir* **28** 5513–7
[18] Tulina N A, Borisenko I Y, Shmytko I M, Ionov A M, Kolesnikov N N and Borisenko D N 2012 Induced non-metallicity during resistive switching in structures based on a topological insulator Bi2Se3 *Phys. Lett.* A **376** 3398–401
[19] Tulina N A, Rossolenko A N, Shmytko I M, Kolesnikov N N, Borisenko D N, Sirotkin V V and Borisenko I Y 2016 Frequency properties of heterostructures based on bismuth selenide upon bipolar resistive switching: experiments and numerical simulation *Bull. Russ. Acad. Sci.* **80** 672–4
[20] Glatz W, Muntwyler S and Hierold C 2006 Optimization and fabrication of thick flexible polymer based micro thermoelectric generator *Sens. Actuators* A **132** 337–45
[21] Schwarzacher W 2006 Electrodeposition: a technology for the future *Electrochem. Soc. Interface* **15** 32–3
[22] Rostek R, Stein N and Boulanger C 2015 A review of electroplating for V–VI thermoelectric films: from synthesis to device integration *J. Mater. Res.* **30** 2518–43
[23] Zampolli S *et al* 2008 Ultra-low-power components for an RFID Tag with physical and chemical sensors *Microsyst. Technol.* **14** 581–8
[24] Ham S, Jeon S, Park M, Choi S, Paeng K J, Myung N and Rajeshwar K 2010 Electrodeposition and stripping analysis of bismuth selenide thin films using combined electrochemical quartz crystal microgravimetry and stripping voltammetry *J. Electroanal. Chem.* **638** 195–203
[25] Ahmed R, Lin Q, Xu Y and Zangari G 2019 Growth, morphology and crystal structure of electrodeposited Bi2 Se3 films: influence of the substrate *Electrochim. Acta* **299** 654–62
[26] Chiu F 2014 A review on conduction mechanisms in dielectric films *Adv. Mater. Sci. Eng.* **2014** 578168
[27] Zhu Y B, Zheng K, Wu X and Ang L K 2017 Enhanced stability of filament-type resistive switching by interface engineering *Sci. Rep.* **7** 2–8
[28] Martinez G *et al* 2017 Determination of the energy band gap of Bi 2 Se 3 *Sci. Rep.* **7** 1–5
[29] Majhi K, Pal K, Lohani H, Banerjee A, Mishra P, Yadav A K, Ganesan R, Sekhar B R, Waghmare U V and Anil Kumar P S 2017 Emergence of a weak topological insulator from the BixSey family *Appl. Phys. Lett.* **110** 162102

[30] Kirchhoff F, Holender J and Gillan M 1996 Structure, dynamics, and electronic structure of liquid Ag-Se alloys investigated by *ab initio* simulation *Phys. Rev.* B **54** 190–202
[31] Guin S N, Srihari V and Biswas K 2015 Promising thermoelectric performance in n-type AgBiSe2: effect of aliovalent anion doping *J. Mater. Chem.* A **3** 648–55
[32] Jupnik H 1941 Photoelectric properties of bismuth *Phys. Rev.* **60** 884–9
[33] Qu J *et al* 2018 Intraband mid-infrared transitions in Ag2Se nanocrystals: potential and limitations for Hg-free low-cost photodetection *J. Phys. Chem.* C **122** 18161–7
[34] Sun W, Gao B, Chi M, Xia Q, Yang J J, Qian H and Wu H 2019 Understanding memristive switching via *in situ* characterization and device modeling *Nat. Commun.* **10** 1–13
[35] Waser R, Dittmann R, Staikov C and Szot K 2009 Redox-based resistive switching memories nanoionic mechanisms, prospects, and challenges *Adv. Mater.* **21** 2632–63
[36] Tulina N A, Rossolenko A N, Shmytko I M, Kolesnikov N N, Borisenko D N, Bozhko S I and Ionov A M 2015 Rectification and resistive switching in mesoscopic heterostructures based on Bi2Se3 *Mater. Lett.* **158** 403–5
[37] Pan F, Gao S, Chen C, Song C and Zeng F 2014 Recent progress in resistive random access memories: materials, switching mechanisms, and performance *Mater. Sci. Eng.* R **83** 1–59
[38] Takagaki Y, Ramsteiner M, Jahn U, Jenichen B and Trampert A 2019 Memristive resistive switch based on spontaneous barrier creation in metal-chalcogenide junctions *J. Phys. D: Appl. Phys.* **52** 385101
[39] Takagaki Y, Jahn U, Ramsteiner M and Friedland K J 2011 Substitution of bismuth in hot wall epitaxy of Bi2Se3 on transition metals *Semicond. Sci. Technol.* **26** 1–6
[40] Walsh L A, Smyth C M, Barton A T, Wang Q, Che Z, Yue R, Kim J, Kim M J, Wallace R M and Hinkle C L 2017 Interface chemistry of contact metals and ferromagnets on the topological insulator Bi2Se3 *J. Phys. Chem.* C **121** 23551–63
[41] Liu N, Yan P, Li Y, Lu K, Sun H J, Ji H K, Xue K H and Miao X S 2018 Conducting mechanism of Ag-diffused Bi–Te based resistive switching devices *Appl. Phys.* A **124** 1–7
[42] Soni R, Meuffels P, Staikov G, Weng R, Kügeler C, Petraru A, Hambe M, Waser R and Kohlstedt H 2011 On the stochastic nature of resistive switching in Cu doped Ge 0.3Se0.7 based memory devices. J *Appl. Phys.* **110** 054509
[43] Ye M, Technology I, Eremeev S V and Kuroda K 2011 Relocation of the topological surface state of Bi2Se3 beneath the surface by Ag intercalation (arXiv:1112.5869)
[44] Koski K J, Wessells C D, Reed B W, Cha J J, Kong D and Cui Y 2012 Chemical intercalation of zerovalent metals into 2D layered Bi 2Se 3 nanoribbons *J. Am. Chem. Soc.* **134** 13773–9
[45] Uesugi E *et al* 2019 Fermi level tuning of Ag-doped Bi 2 Se 3 topological insulator *Sci. Rep.* **9** 3–10
[46] Ferfolja K, Valant M, Mikulska I, Gardonio S and Fanetti M 2018 Chemical instability of an interface between silver and Bi2Se3 topological insulator at room temperature *J. Phys. Chem.* C **122** 9980–4
[47] Kang Y H, Choi J H, Il Lee T, Lee W and Myoung J M 2011 Thickness dependence of the resistive switching behavior of nonvolatile memory device structures based on undoped ZnO films *Solid State Commun.* **151** 1739–42
[48] Liu J *et al* 2018 Analysis of tail bits generation of multilevel storage in resistive switching memory *Chin. Phys.* B **27** 118501
[49] Kong D *et al* 2011 Rapid surface oxidation as a source of surface degradation factor for Bi2Se3 *ACS Nano* **5** 4698–703
[50] Edmonds M T, Hellerstedt J T, Tadich A, Schenk A, Odonnell K M, Tosado J, Butch N P, Syers P, Paglione J and Fuhrer M S 2014 Stability and surface reconstruction of topological insulator Bi2Se3 on exposure to atmosphere *J. Phys. Chem.* C **118** 20413–9
[51] Mayer T, Klein A, Lang O, Pettenkofer C and Jaegermann W 1992 H2O adsorption on the layered chalcogenide semiconductors WSe2, InSe and GaSe *Surf. Sci.* **269–270** 909–14 91368–L
[52] Blanco Carballo V M, Melai J, Salm C and Schmitz J 2009 Moisture resistance of SU-8 and KMPR as structural material *Microelectron. Eng.* **86** 765–8
[53] Kim M, Yoo K, Jeon S P, Park S K and Kim Y H 2020 The effect of multi-layer stacking sequence of TiOx active layers on the resistive-switching characteristics of memristor devices *Micromachines* **11** 154
[54] Mohammad B, Jaoude M A, Kumar V, Al Homouz D M, Nahla H A, Al-Qutayri M and Christoforou N 2016 State of the art of metal oxide memristor devices *Nanotechnol. Rev.* **5** 311–29